Appendix to "Estimation of Crust and Lithospheric Properties for Mercury from High-Resolution Gravity and Topography"

Sander Goossens,[1] Antonio Genova,[2] Peter B. James,[3] and Erwan Mazarico[1]

[1] *NASA Goddard Space Flight Center, Greenbelt, Maryland, USA.*
[2] *Sapienza, University of Rome, Department of Mechanical and Aerospace Engineering, Rome, Italy.*
[3] *Department of Geosciences, Baylor University, Waco, TX, USA.*

INTRODUCTION

This is the appendix to our paper "Estimation of Crust and Lithospheric Properties for Mercury from High-Resolution Gravity and Topography", published in *The Planetary Sience Journal*. The appendix consists of two parts: first, in Section A, we include the equations that describe the admittance model of Grott & Wieczorek (2012) that we used, for completeness. Second, in Section B, we include additional figures that are referenced in the main text.

APPENDIX

A. ADMITTANCE MODEL

We use the admittance model of Grott & Wieczorek (2012) without modifications, and for completeness we repeat the equations here.

The gravitational potential is expressed in spherical harmonics with coefficients g_{nm} and topography with coefficients h_{nm}, where n is the degree and m the order. Here, g_{nm} relates to $\bar{C}_{nm}$ for $m \geq 0$ and to $\bar{S}_{nm}$ for $m < 0$. Admittance Q_n is isotropic and only dependent on the degree, and it expresses the transfer function between gravity and topography, such that $g_{nm} = Q_n h_{nm}$.

Grott & Wieczorek (2012) include both surface loading, indicated with Q_n^s and sub-surface loading, indicated with Q_n^z. The equation for Q_n^s is given by

$$Q_n^s = \frac{3 g_0 \rho_l}{\bar{\rho}(2n+1)} \left[\frac{1 - C_n^s \frac{\rho_c}{\rho_m} - C_n^s \frac{\rho_m - \rho_c}{\rho_m} \left(\frac{a_e - T_c}{a_e} \right)^{(n+2)}}{1 - C_n^s \frac{\rho_l}{\rho_m}} \right], \tag{A1}$$

where g_0 is the surface gravitational acceleration, ρ_l is the load density, ρ_c is the crustal density, ρ_m is the mantle density, a_e is the planet's mean radius, T_c the crustal thickness, and C_n^s is given by

$$C_n^s = \frac{\rho_m}{\rho_m - \rho_c} \frac{\bar{C}_n^s}{\left(1 + \frac{\rho_c}{\rho_m - \rho_c} \bar{C}_n^s\right)}, \tag{A2}$$

with $\bar{C}_n^s$ determined from the thin-shell flexure equation (*e.g.* Turcotte et al. 1981) and a model for the gravitational force acting on the lithosphere, following

$$\bar{C}_n^s = \frac{\left[1 - \frac{3\rho_c}{\bar{\rho}(2n+1)} - \frac{3(\rho_m - \rho_c)}{\bar{\rho}(2n+1)} \left(\frac{a_e - T_c}{a_e}\right)^n\right]}{\left[\frac{g_m}{g_0} - \frac{1}{\xi g_0 (\rho_m - \rho_c)} - \frac{3\rho_c}{\bar{\rho}(2n+1)} \left(\frac{a_e - T_c}{a_e}\right)^{(n+2)} - \frac{3(\rho_m - \rho_c)}{\bar{\rho}(2n+1)} \left(\frac{a_e - T_c}{a_e}\right)\right]}. \tag{A3}$$

Here, $\bar{\rho}$ is the average density of the planet, and g_m is the gravitational acceleration at the crust-mantle interface. We compute the latter by assuming a planet in hydrostatic equilibrium with a constant crustal density. Gravity $g(r)$ at a

Corresponding author: Sander Goossens
sander.j.goossens@nasa.gov

radius r inside a planet with radius a_e in hydrostatic equilibrium can be expressed as (*e.g.* Turcotte & Schubert 2002)

$$g(r) = \frac{4\pi G}{r^2} \int_0^r \rho(r')r'^2 \; dr', \tag{A4}$$

where G is the gravitational constant. At the base of the crust, $r = a_e - T_c$ and $g(a_e - T_c)$ can be obtained from

$$g(a_e - T_c) = \frac{4\pi G}{(a_e - T_c)^2} \left[\int_0^{a_e} \rho(r')r'^2 \; dr' - \int_{a_e - T_c}^{a_e} \rho(r')r'^2 \; dr' \right]. \tag{A5}$$

The first integral can be related to gravity at the surface g_0, as

$$\begin{aligned} g_0 = g(a_e) &= \frac{4\pi G}{{a_e}^2} \int_0^{a_e} \rho(r')r'^2 \; dr'; \\ \int_0^{a_e} \rho(r')r'^2 \; dr' &= g_0 \frac{{a_e}^2}{4\pi G}. \end{aligned} \tag{A6}$$

For the second integral a constant density ρ_c is assumed. In that case, the second integral can be expressed analytically, following

$$\int_{a_e - T_c}^{a_e} \rho(r')r'^2 \; dr' = \rho_c \left[\frac{1}{3} r^3 \right]_{a_e - T_c}^{a_e} = \frac{\rho_c}{3} \left(a_e^3 - (a_e - T_c)^3 \right). \tag{A7}$$

Finally, gravity at the base of the crust, g_m ,becomes

$$g_m = g(a_e - T_c) = \left(\frac{a_e}{a_e - T_c} \right)^2 g_0 - \frac{4\pi G \rho_c}{3(a_e - T_c)^2} \left[a_e^3 - (a_e - T_c)^3 \right]. \tag{A8}$$

An extension to include a depth z in the mantle can be made readily by assuming a constant mantle density.

In equation A3, ξ is defined as

$$\xi = -\frac{R_e^4 \left[n(n+1) - 1 + \nu \right]}{D\tilde{n}^3 + 2D\tilde{n}^2 + ET_e R_e^2 \tilde{n}} \tag{A9}$$

, with $\tilde{n} = n(n+1) - 2$ and $R_e = a_e - \frac{1}{2}T_c$. D is the flexure parameter defined as

$$D = \frac{ET_e^3}{12(1-\nu^2)}, \tag{A10}$$

where E is Young's modulus, T_e elastic thickness, and ν the Poisson ratio.

For sub-surface loading, a load below the surface at a depth z is considered. Q_n^z is given by

$$Q_n^z = \frac{3 g_0 \rho_c}{\bar{\rho}(2n+1)} \left[\left(\frac{a_e - z}{a_e} \right)^{(n+2)} - C_n^z \frac{\rho_c}{\rho_m} - C_n^z \frac{\rho_m - \rho_c}{\rho_m} \left(\frac{a_e - T_c}{a_e} \right)^{(n+2)} \right], \tag{A11}$$

where now C_n^z is defined by

$$C_n^z = \frac{\frac{\rho_m}{\rho_m - \rho_c} \phi_1}{\phi_2}, \tag{A12}$$

where

$$\phi_1 = \left[\frac{g_z}{g_0} - \frac{3\rho_c}{\bar{\rho}(2n+1)} \left(\frac{a_e - z}{a_e} \right)^{(n+2)} - \frac{3(\rho_m - \rho_c)}{\bar{\rho}(2n+1)} \left(\frac{a_e - z}{a_e} \right) \left(\frac{a_e - T_c}{a_e - z} \right)^n \right] \tag{A13}$$

and

$$\begin{aligned} \phi_2 = \; & \frac{\rho_c}{\rho_m - \rho_c} + \frac{g_m}{g_0} - \frac{1}{\xi g_0 (\rho_m - \rho_c)} - \\ & \frac{3\rho_c}{\bar{\rho}(2n+1)} \left(\frac{\rho_c}{\rho_m - \rho_c} + \left(\frac{a_e - T_c}{a_e} \right)^{(n+2)} + \frac{\rho_m - \rho_c}{\rho_c} \left(\frac{a_e - T_c}{a_e} \right) + \left(\frac{a_e - T_c}{a_e} \right)^n \right). \end{aligned} \tag{A14}$$

These expressions for ϕ_1 and ϕ_2 are valid for $z \leq T_c$. If the load is below the crust, Grott & Wieczorek (2012) indicate that the last term in ϕ_1 should be changed following

$$\left(\frac{a_e - T_c}{a_e - z}\right)^n \rightarrow \left(\frac{a_e - z}{a_e - T_c}\right)^{(n+1)}. \tag{A15}$$

The parameter g_z is the gravitational acceleration at the depth of the load, which we compute in the same way as g_m from equation A8.

Finally, the model for combined surface and sub-surface loading is defined as having a transfer function Q_n given by

$$Q_n = \frac{Q_n^s + Q_n^z \frac{\rho_l}{\rho_c}\left(1 - X_n^s\right) f_{nm}}{1 - C_n^z \frac{\rho_l}{\rho_m}\left(1 - X_n^s\right) f_{nm}}, \tag{A16}$$

where

$$X_n^s = \frac{C_n^s \frac{\rho_l}{\rho_m}}{C_n^s \frac{\rho_l}{\rho_m} - 1}, \tag{A17}$$

and where f_{nm} is the load ratio between bottom and top loading. A thin mass sheet approximation with surface density σ_{nm} is used for loading, and f_{nm} is then given by

$$f_{nm} = \frac{\sigma_{nm}^z}{\sigma_{nm}^s}, \tag{A18}$$

where superscripts s and z stand for loading at the surface or at depth, respectively. For values of f_{nm} of $\pm\infty$ there is bottom loading only, whereas $f_{nm} = 0$ corresponds to top-loading only. For convenience, a loading parameter L_{nm} is defined such that

$$L_{nm} = \frac{f_{nm}}{1 + |f_{nm}|}. \tag{A19}$$

This is now bounded between -1 and 1, and $L_{nm} = 0$ corresponds to top loading only, and for $f_{nm} = -1$, a state of isostasy where the bottom load is equal to the top load but of opposite sign, $L_{nm} = -1/2$. Furthermore, f_{nm} is assumed to be isotropic, and thus independent of degree and order, which means that f_{nm} and L_{nm} revert to f and L.

B. ADDITIONAL FIGURES

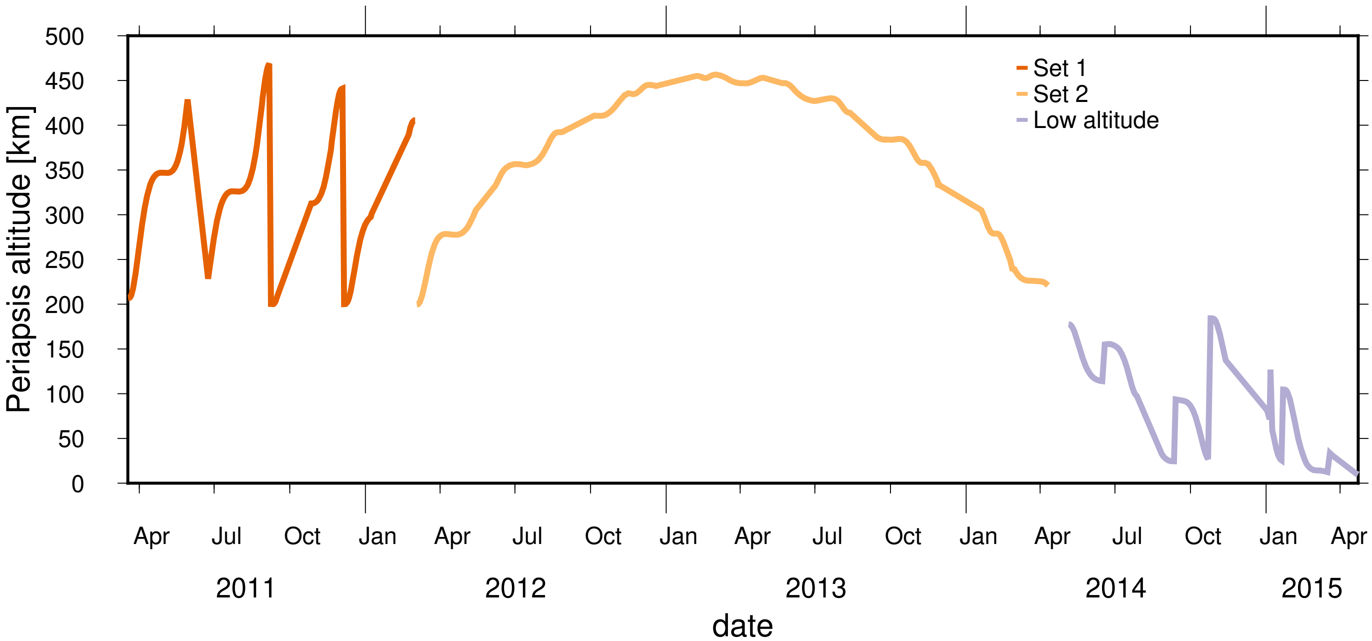

Figure A1. The altitude of MESSENGER's periapsis throughout the mission. We use this to divide the tracking data into three statistical sets, for which we additionally estimate scale factors when determining the gravity field, using variance component estimation (Kusche 2003). These scale factors are listed in Table ??.

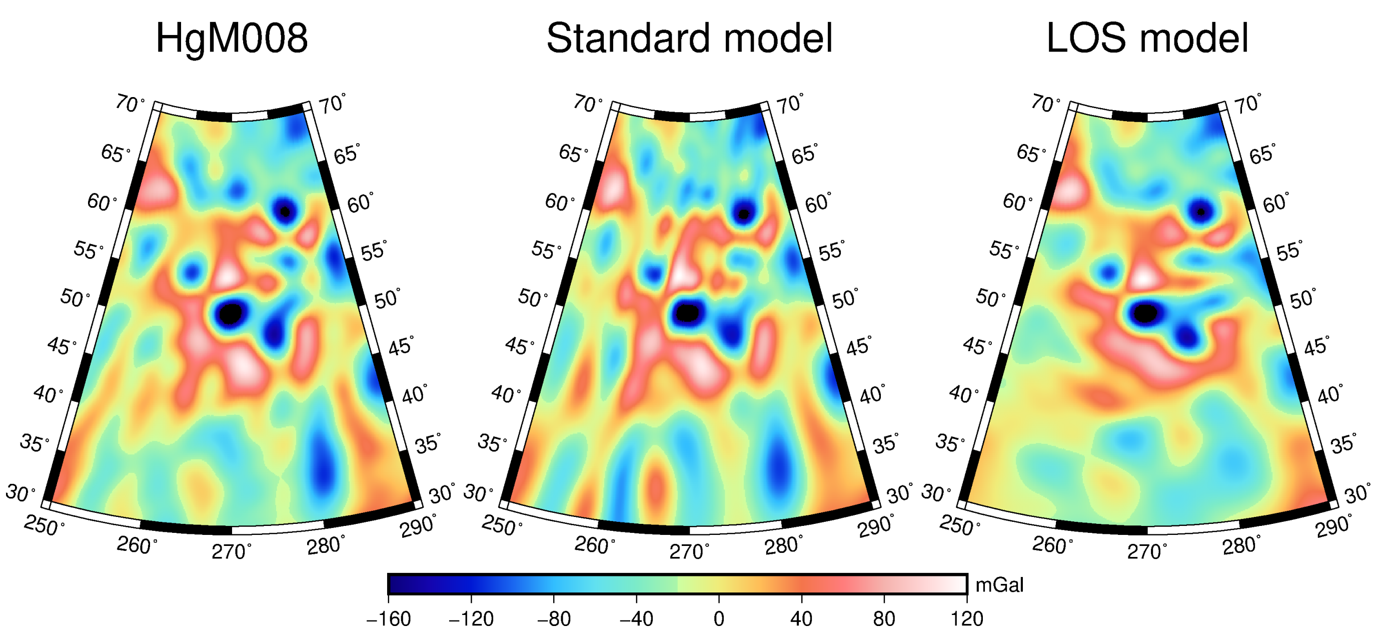

Figure A2. Gravity anomalies for the area with low-altitude data, centered on 270°E, 50°N, for various gravity field models: HgM008, the standard model, and the LOS model. Despite very similar gravity anomaly maps, correlations between gravity and topography for the standard model are lower than those for HgM008, due to some remaining spurious signal in the solution. The LOS model has a different look, and improved correlations with topography. The map is in a Lambert Conformal Conic projection.

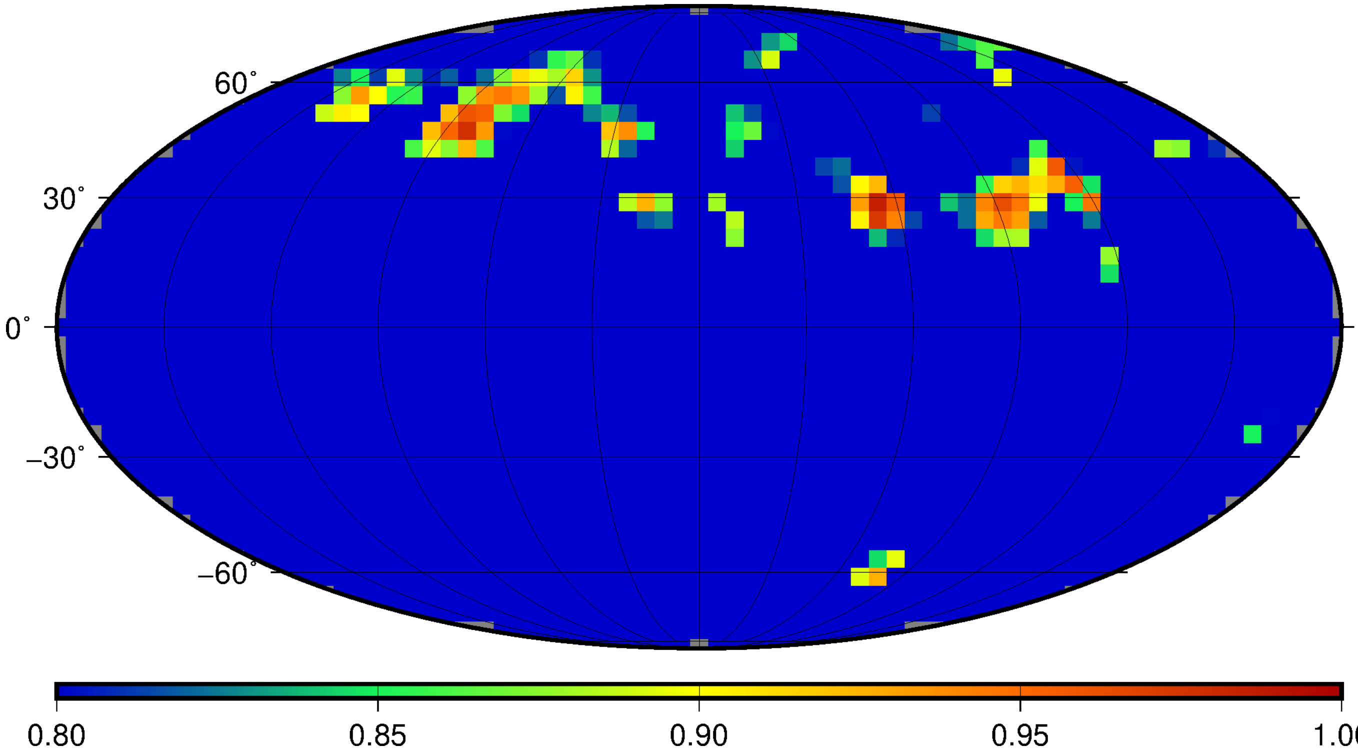

Figure A3. Averaged correlations weighted by their deviation from 1.0. The map is in Mollweide projection centered on the prime meridian.

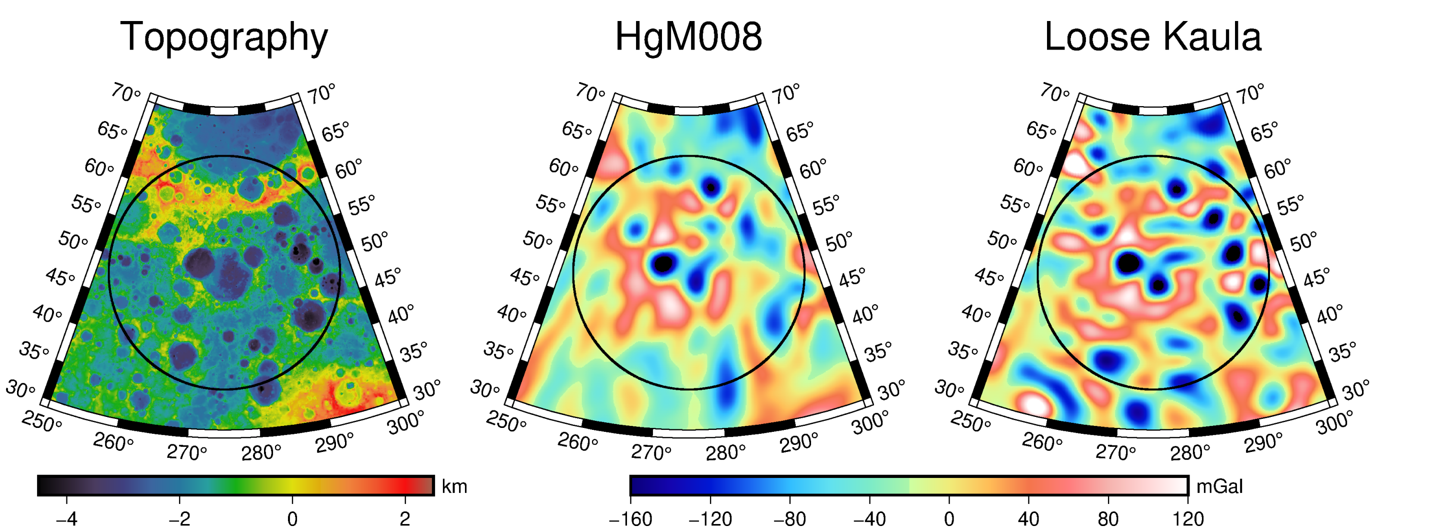

Figure A4. Topography, and gravity anomalies for the HgM008 and LOS model (with loose Kaula), for area 1 which is centered on 275°E, 50°N. We indicate the localization area in the admittance analysis with a circle. The map is in a Lambert Conformal Conic projection.

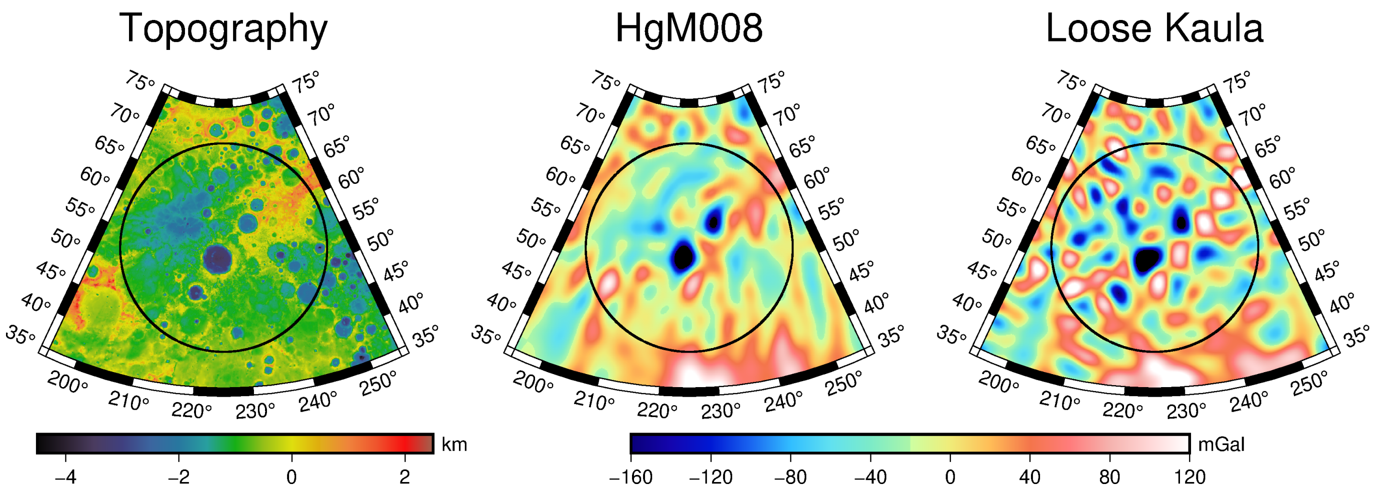

Figure A5. Topography, and gravity anomalies for the HgM008 and LOS model (with loose Kaula), for area 2 which is centered on 225°E, 55°N. We indicate the localization area in the admittance analysis with a circle. The map is in a Lambert Conformal Conic projection.

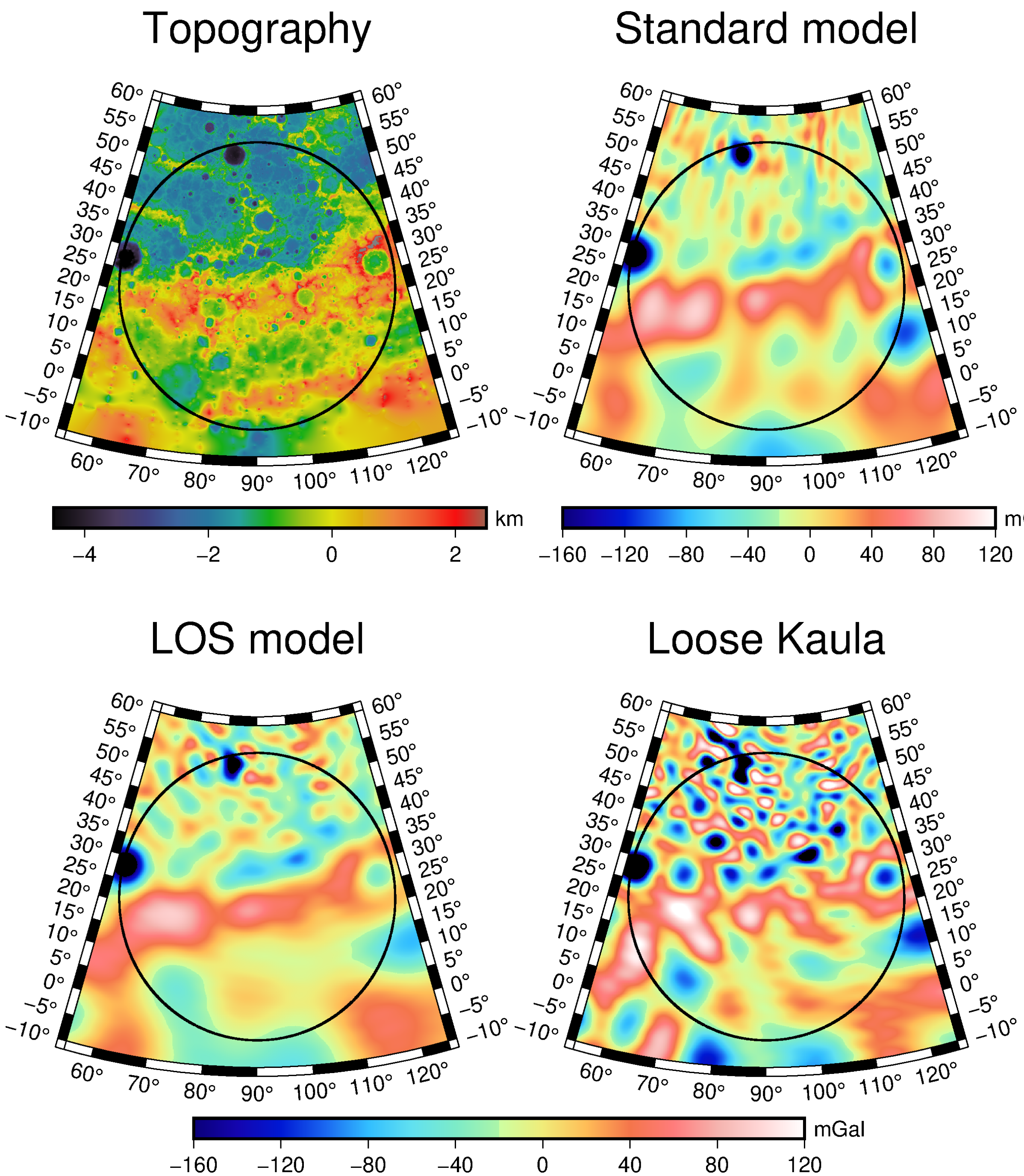

Figure A6. Topography, and gravity anomalies for various models for area 3 which is centered on 90°E, 25°N. We indicate the localization area in the admittance analysis with a circle. A cap with a radius of 30° was used for this area. We include the various models in this plot, and used the Standard model (with a resolution of degree and order 180) in the admittance analysis. The map is in a Lambert Conformal Conic projection.

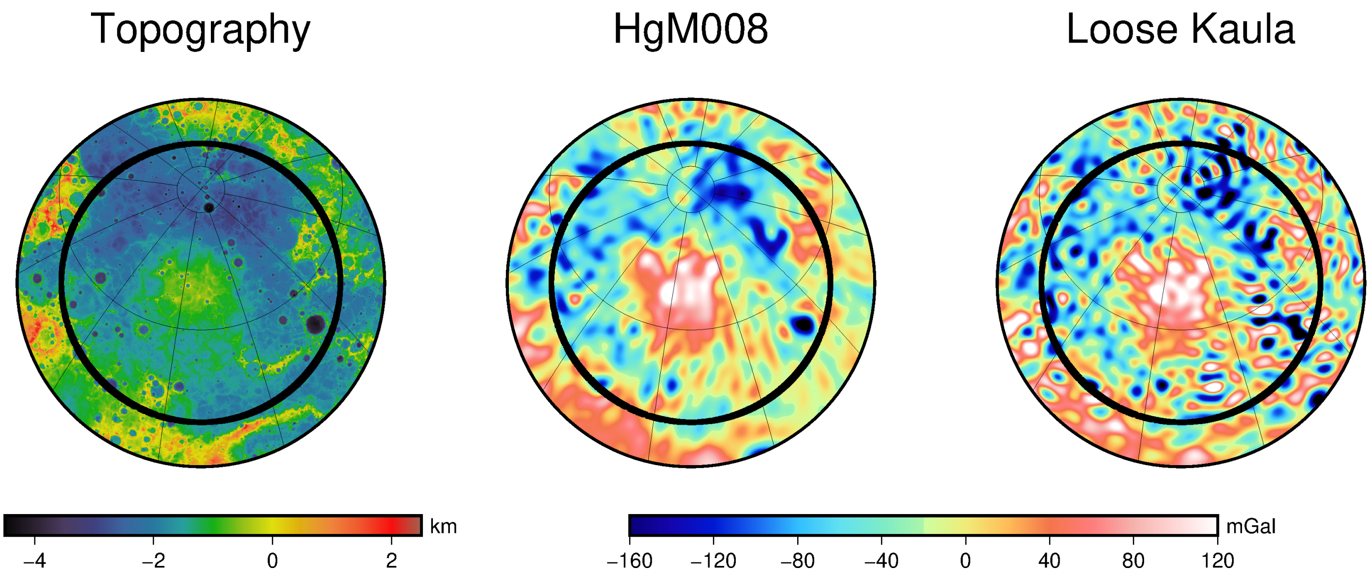

Figure A7. Topography, and gravity anomalies for the HgM008 and LOS model (with loose Kaula), for area 4 which is centered on 40°E, 70°N. We indicate the localization area in the admittance analysis with a circle. A cap radius of 30° was used for the localization. The map is in a Lambert Azimuthal Equal Area projection because the cap partly covers the north pole.

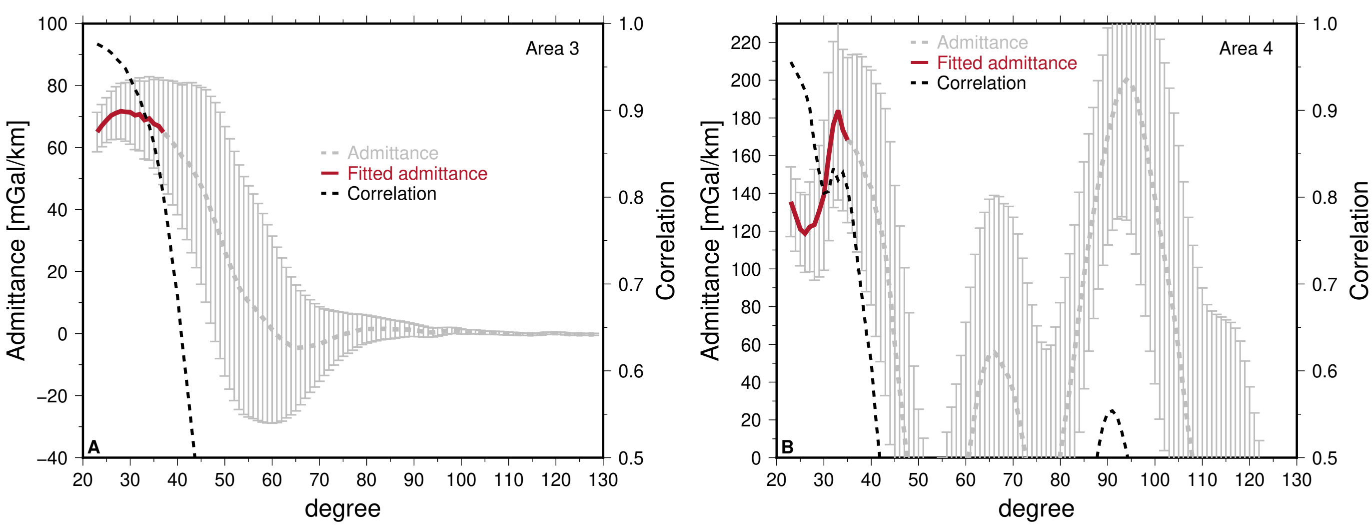

Figure A8. Localized admittance and correlation spectra for areas 3 (A) and 4 (B) when using a cap radius of 15° and $L_{\mathrm{win}} = 22$. The range of degrees with correlations higher than 0.8 is rather limited, and so we opted to use a larger cap radius of 30°, resulting in a smaller L_{win} of 8.

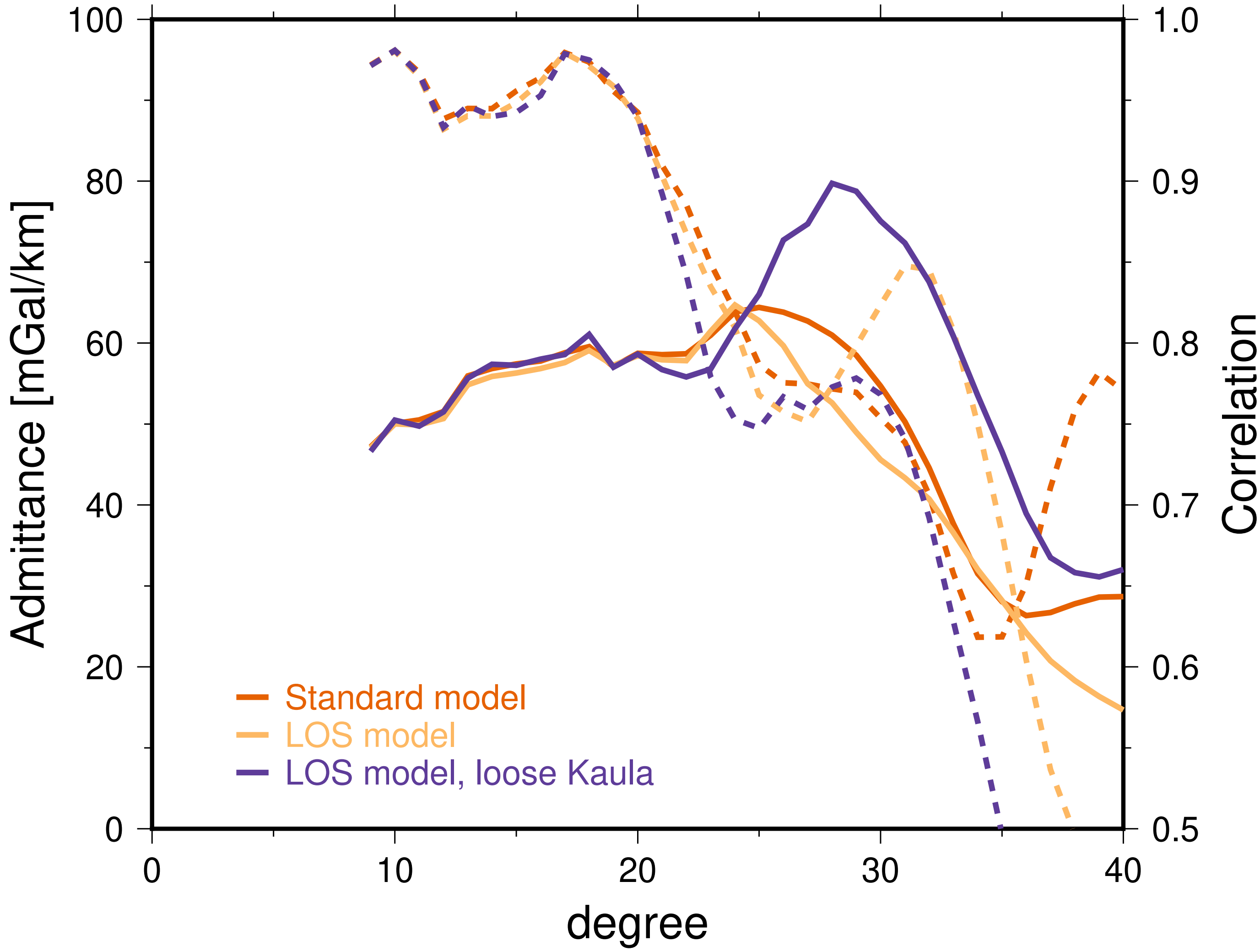

Figure A9. Localized admittance and correlation spectra for area 3 for various models, using $L\text{win} = 8$. Because of relatively high admittance values for the Loose Kaula model, we decided to perform the admittance analysis for area 3 with the Standard Model.

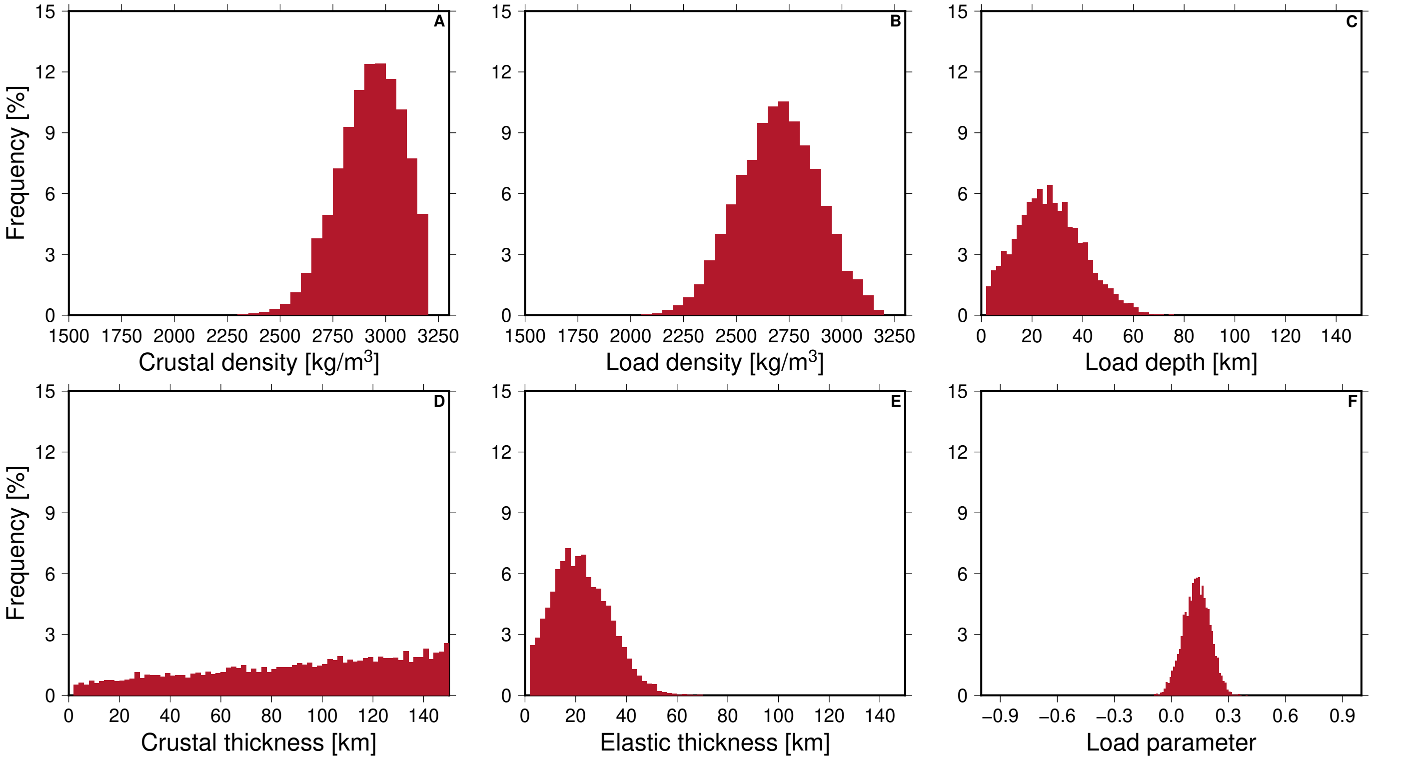

Figure A10. Results from the MCMC analysis for area 4, using the larger cap radius of 30° and $L_{\mathrm{win}} = 8$, where we do not enforce that the load density is larger than the crustal density. In this case, the crustal density sometimes is larger than the load density. Results are shown as *a posteriori* probability distributions for the estimated parameters: crustal density (A), load density (B), load depth (C), crustal thickness (D), elastic thickness (E), and load parameter (F).

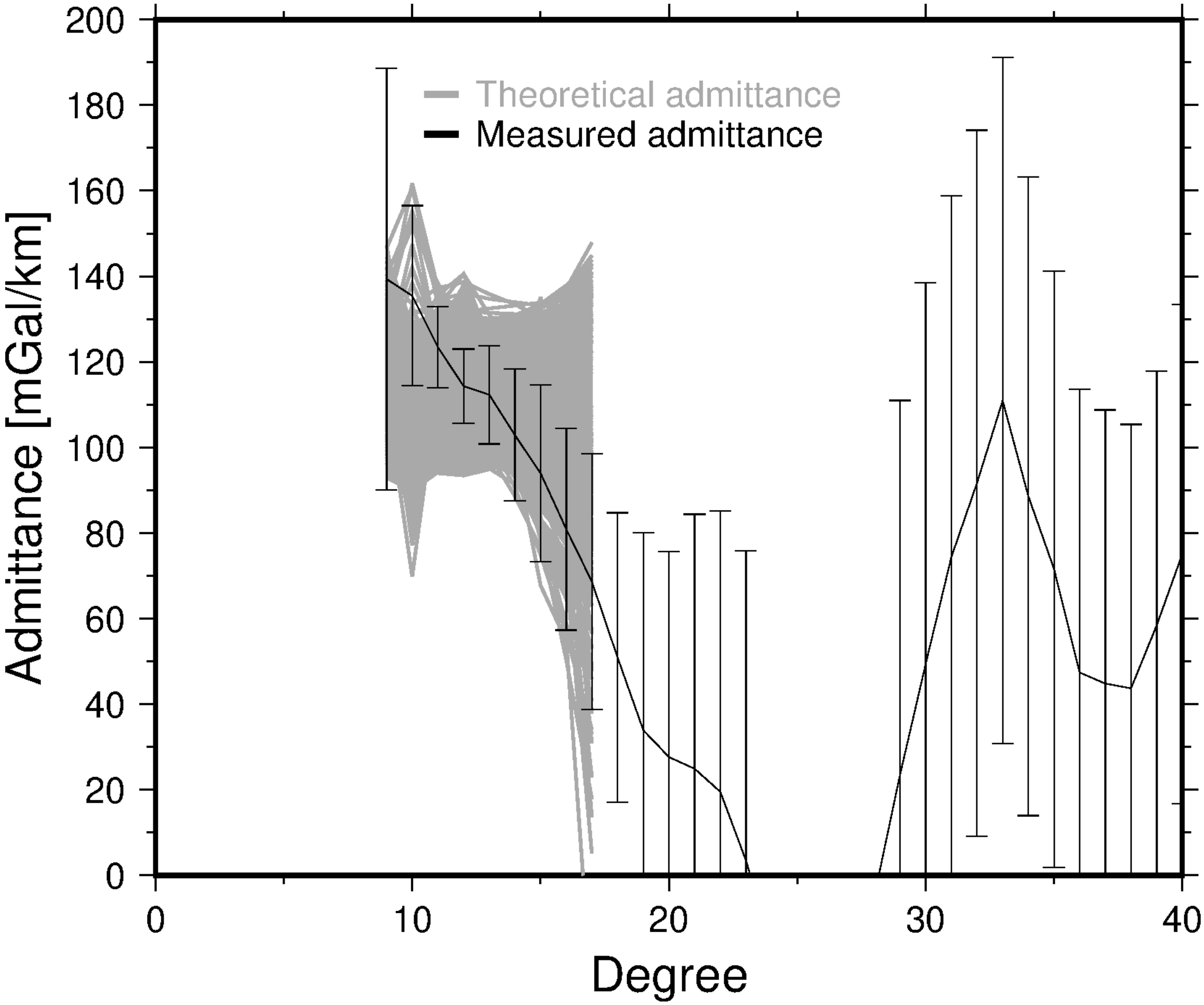

Figure A11. Fitted admittance spectra from the MCMC analysis for area 4, using a cap radius of 30° and $L_{\mathrm{win}} = 8$, where we do not enforce that the load density has to be larger than the crustal density. The admittance fit is nearly the same to the case where we do enforce this (Figure 8D).

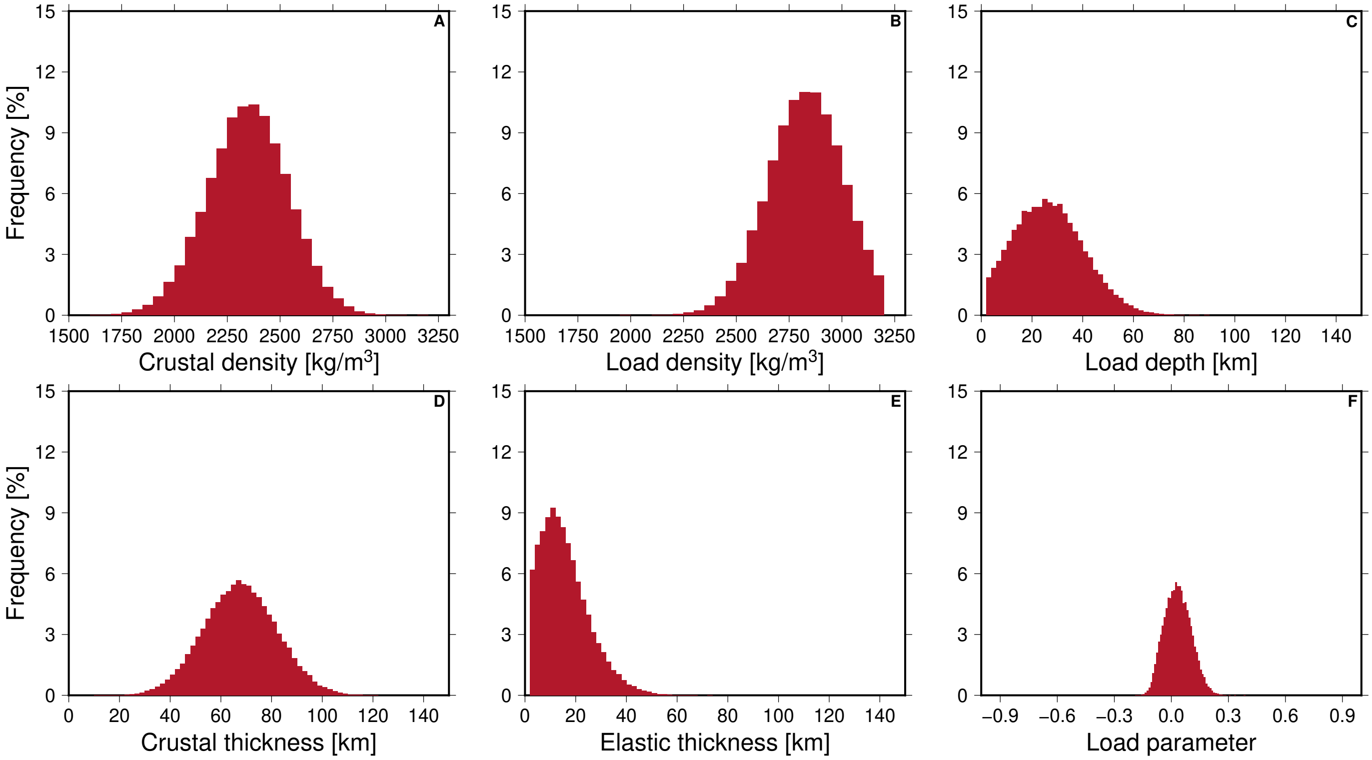

Figure A12. Results from the MCMC analysis for area 4 when using the smaller cap radius of 15° and the value of $L_{\text{win}} = 22$ in the localization. Results are shown as *a posteriori* probability distributions for the estimated parameters: crustal density (A), load density (B), load depth (C), crustal thickness (D), elastic thickness (E), and load parameter (F).

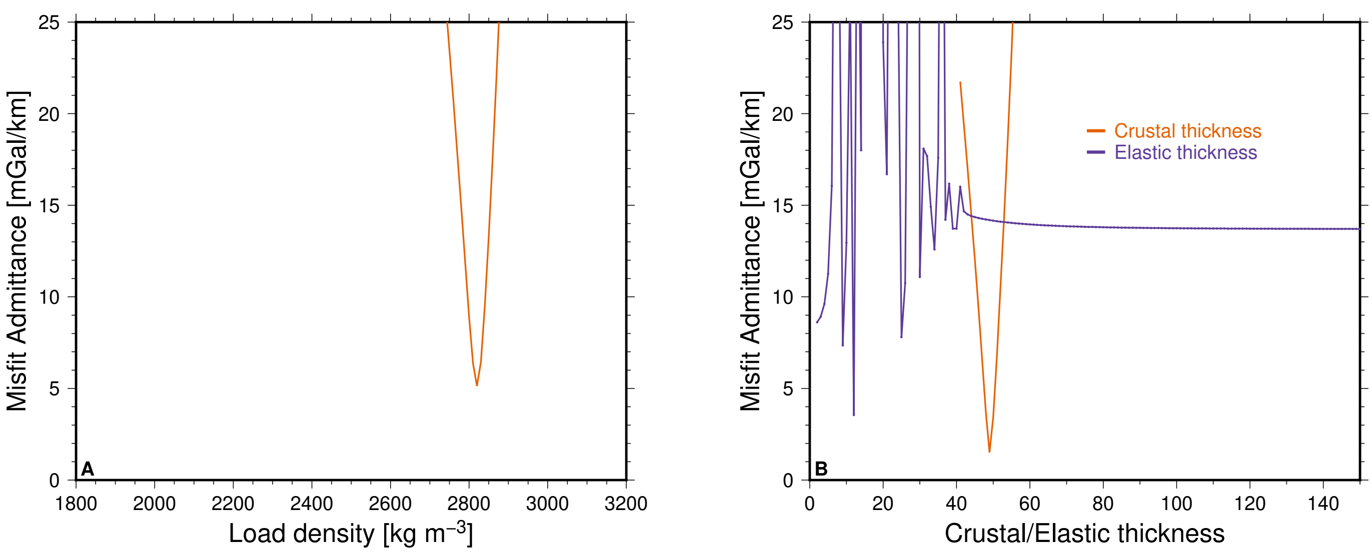

Figure A13. Results from a sensitivity analysis, where we took the model values that produce the best fit to the admittance, and then varied one parameter while keeping the others fixed (at the best-fit value). We show the misfit versus load density for area 4 (A), and misfit versus crustal and elastic thickness for area 2 (B).

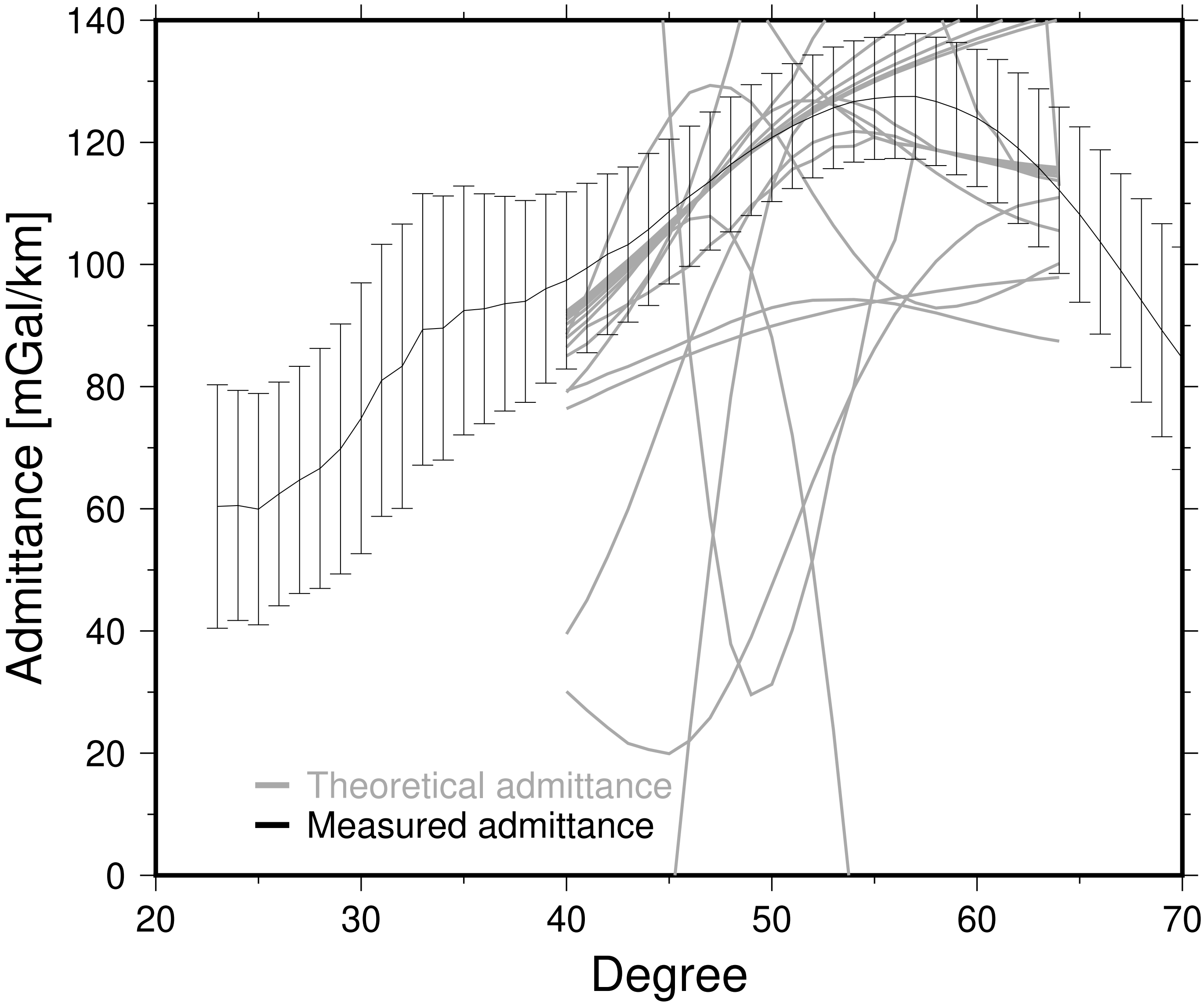

Figure A14. Fitted admittance spectra from the sensitivity analysis from Figure A13, where we varied elastic thickness T_e for area 2. The best fit elastic thickness is close to 12 km. Here we show spectra for T_e values between 2 and 21 km, while we keep the other parameters in the admittance model fixed to the best-fit values. In combination with the other best fit parameters, the spectrum can be very sensitive to the T_e value, hence the wide spread in misfit values in Figure A13B.

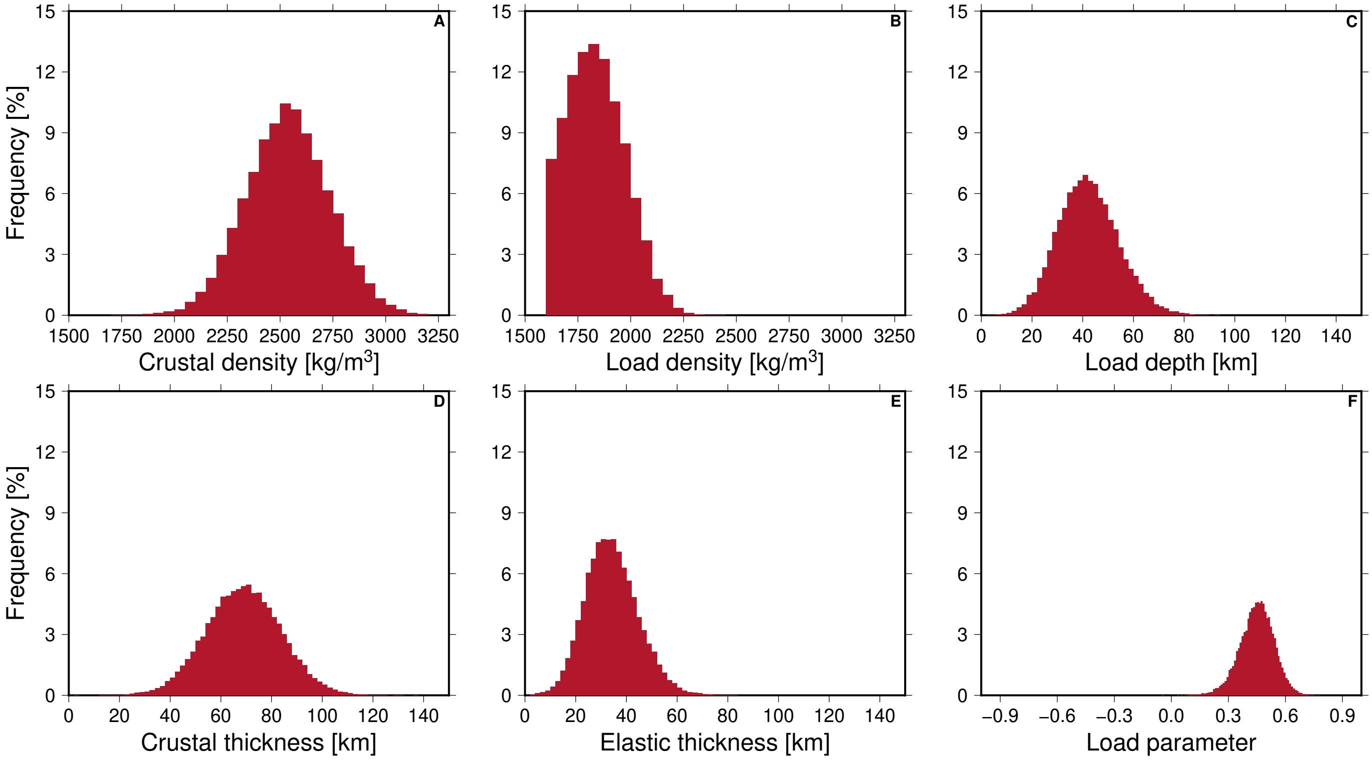

Figure A15. Results from the MCMC analysis for area 1, where we used the limited degree range 40–65 to fit the admittance. The results are shown as *a posteriori* probability distributions for the admittance misfit (A), and the estimated parameters: crustal density (B), crustal or load density (B), load depth (C), crustal thickness (D), elastic thickness (E), and load parameter (F).

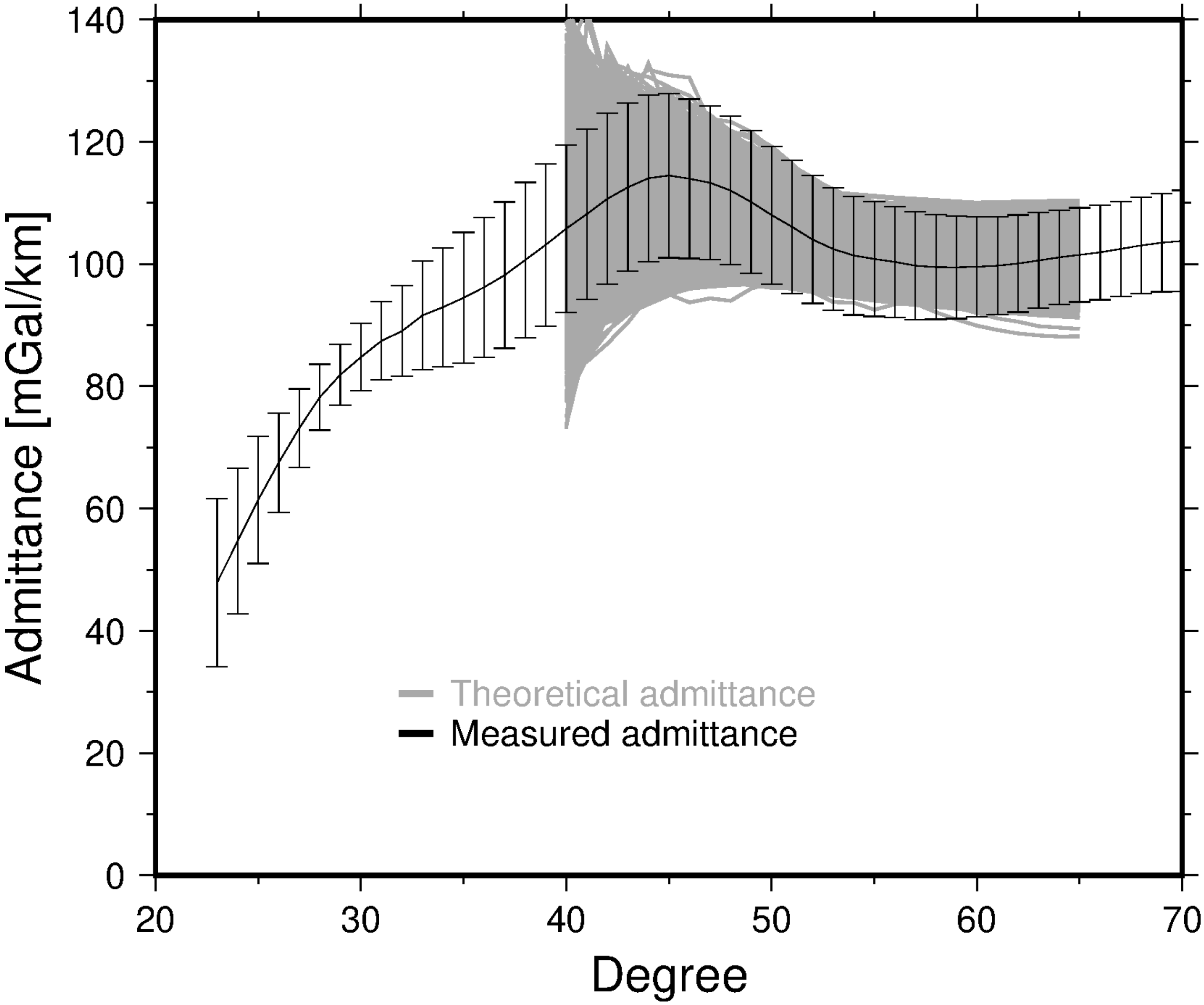

Figure A16. Fitted admittance spectra from the MCMC analysis for area 1 where we fitted the admittance between degrees 40–65. The measured spectra are shown in black, and the spectra for the MCMC models are shown in gray.

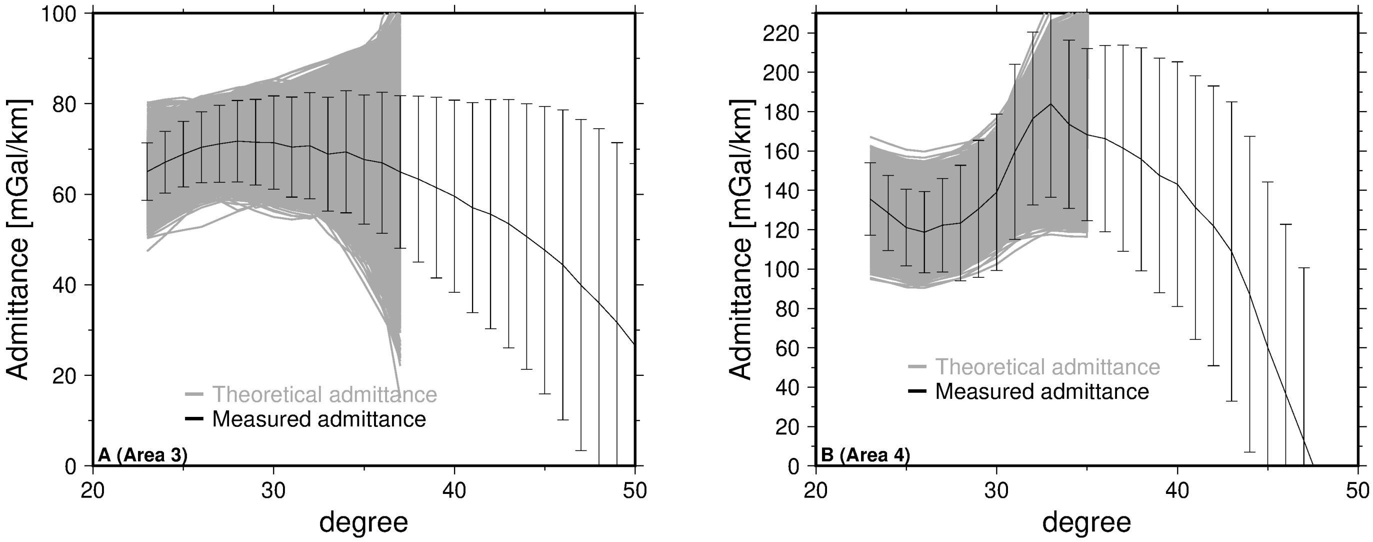

Figure A17. Fitted admittance spectra from our MCMC analysis for areas 3 and 4 when using the smaller localization cap radius of 15° and $L_{\text{win}} = 22$.

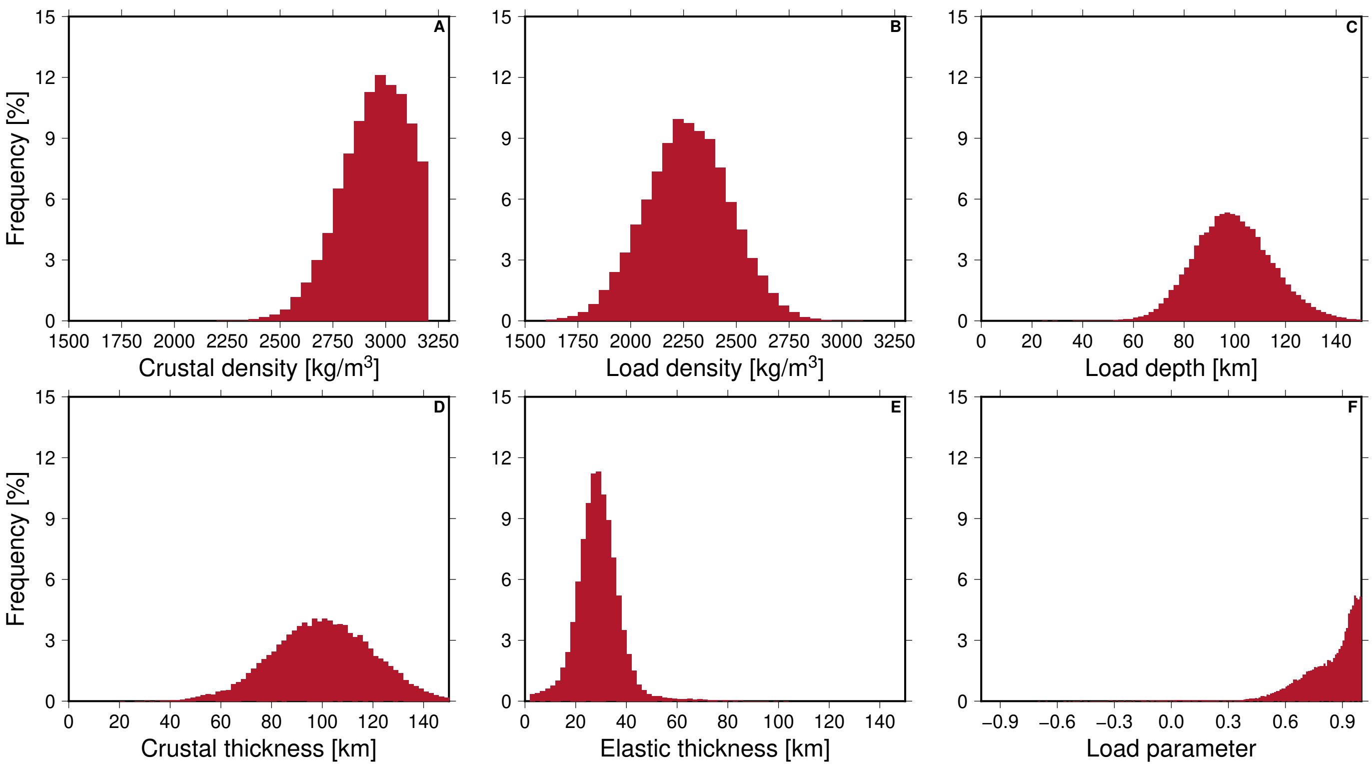

Figure A18. Results from the MCMC analysis for area 3 when using the smaller cap radius of 15° and the value of $L_{\text{win}} = 22$ in the localization. Results are shown as *a posteriori* probability distributions for the estimated parameters: crustal density (A), load density (B), load depth (C), crustal thickness (D), elastic thickness (E), and load parameter (F).

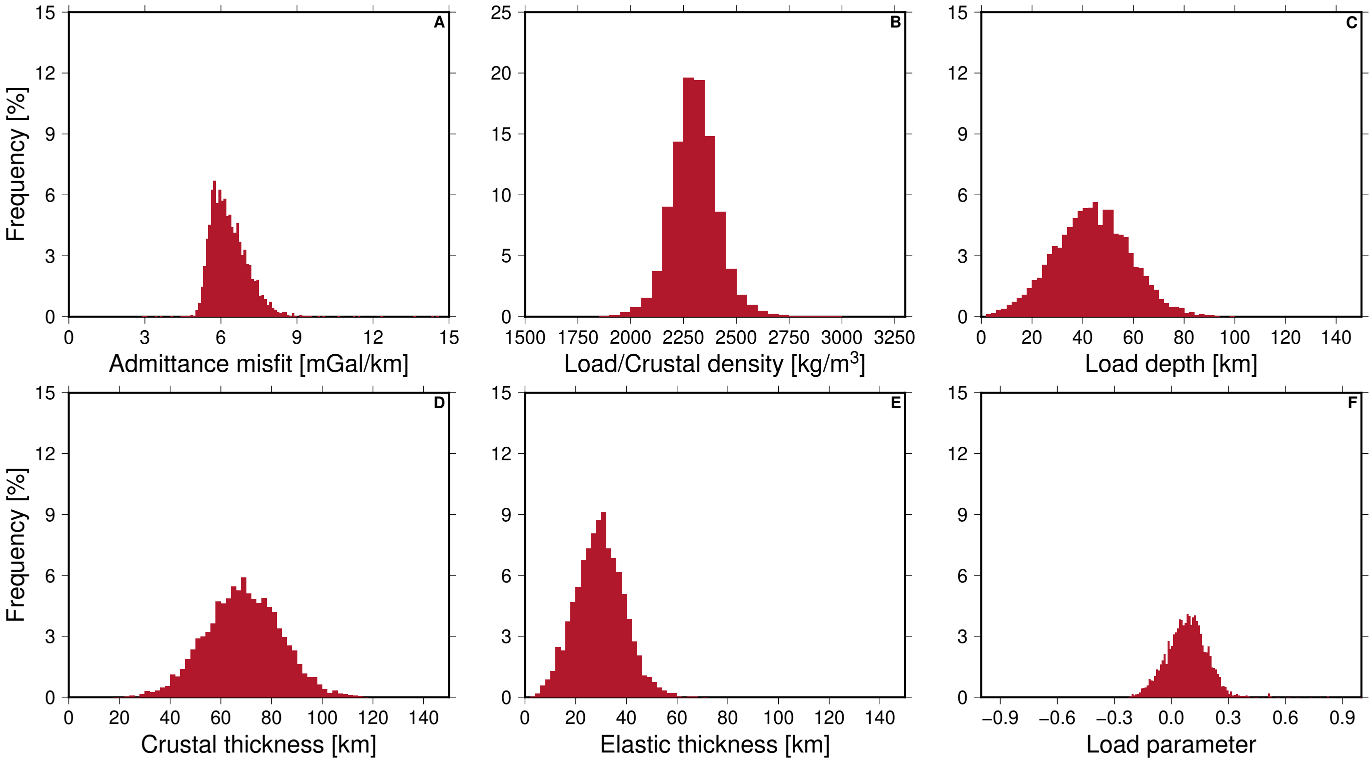

Figure A19. Results from the MCMC analysis for area 1 (using the degree range 30–78 to fit the admittance), where we fixed the load density to be equal to the crustal density. The results are shown as *a posteriori* probability distributions for the admittance misfit (A), and the estimated parameters: crustal density (B), crustal or load density (B), load depth (C), crustal thickness (D), elastic thickness (E), and load parameter (F). For these results, we fixed the load density to be equal to the crustal density.

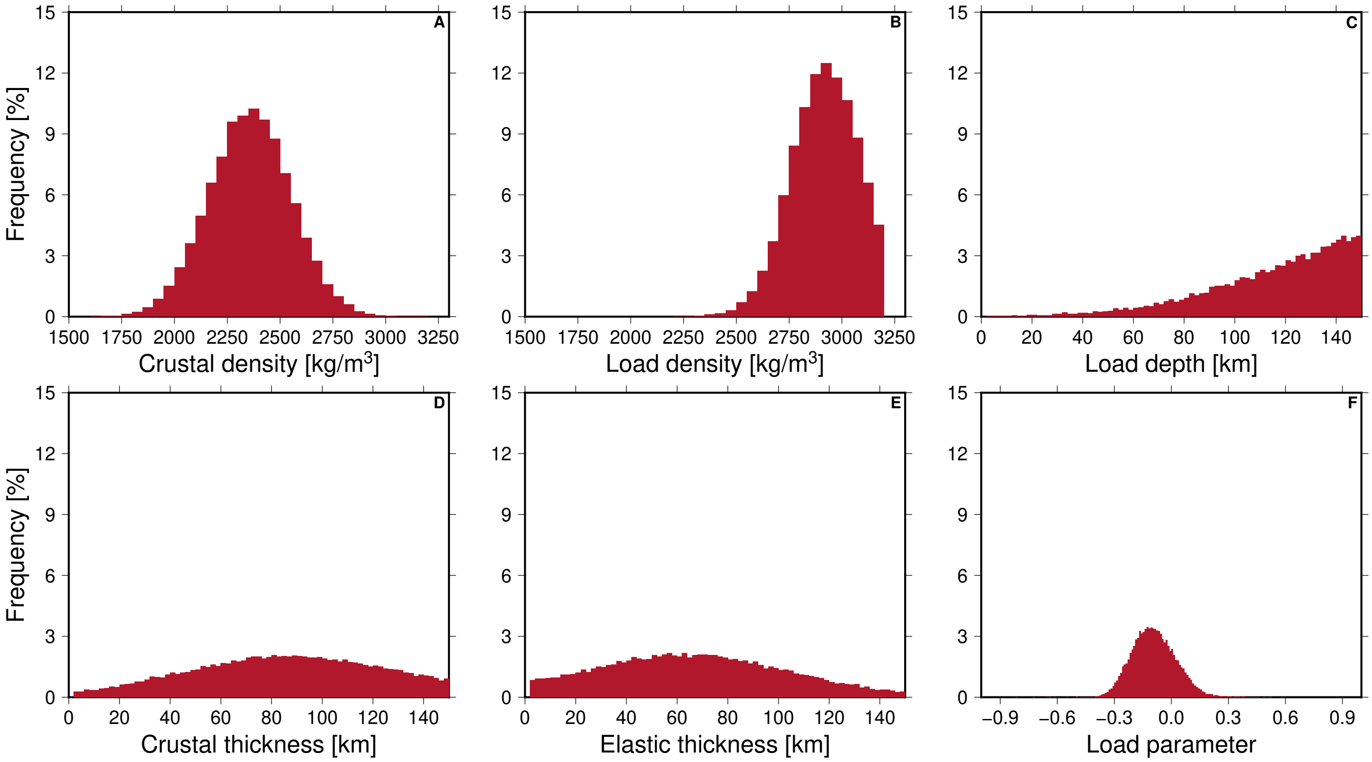

Figure A20. Results from the MCMC analysis for area 4, where we enforce the load to be located in the mantle (which means, for example, a negative load parameter).The results are shown as *a posteriori* probability distributions for the admittance misfit (A), and the estimated parameters: crustal density (B), crustal or load density (B), load depth (C), crustal thickness (D), elastic thickness (E), and load parameter (F).

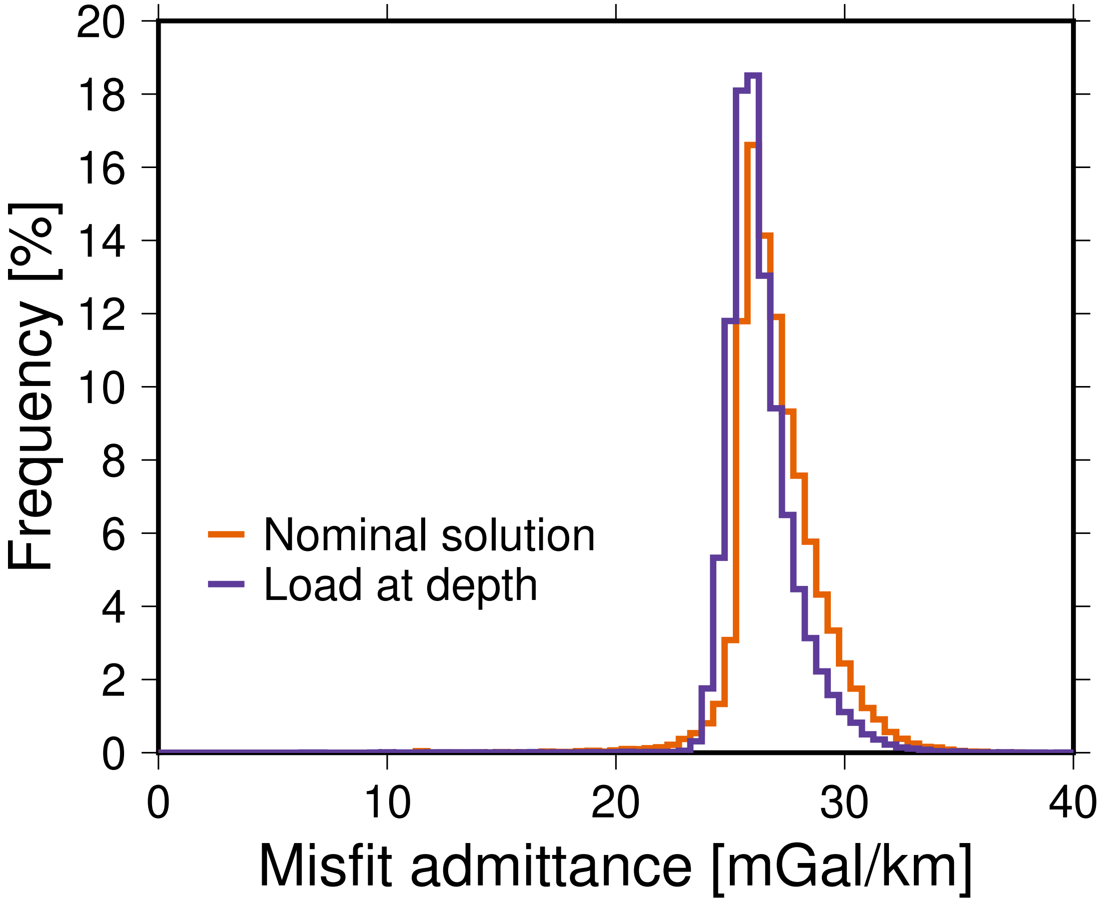

Figure A21. Histogram of the misfit to the admittance for two scenarios for area 4, the northern rise: the nominal solution where we enforce the load density to be larger than the crustal density, which results in mostly top-loading, and the case where the load was enforced at depth.

REFERENCES

Grott, M., & Wieczorek, M. A. 2012, Icarus, 221, 43

Kusche, J. 2003, Advances in Geosciences, 1, 81

Turcotte, D., Willemann, R., Haxby, W., & Norberry, J. 1981, Journal of Geophysical Research, 86, 3951

Turcotte, D. L., & Schubert, G. 2002, Geodynamics (New York, USA: Cambridge University Press)